A FALL DETECTION SYSTEM BASED ON A THERMOPILE IMAGING ARRAY AND A BACK PROJECTION ALGORITHM

Lei Yu[1], Han Chen[1], Hantao He[1], Hong Nie[2], Xuping Zhai[3], Bangshu Xiong[1]

[1] Key Laboratory of Image Processing and Pattern Recognition, Nanchang Hangkong University, Nanchang, China
[2] Department of Technology, University of Northern Iowa, Iowa, 50614-0178, USA
[3] Shanghai University, Shanghai, China

Abstract
In this paper, a fall detection system consisting of a thermopile imaging array with 80*64 pixels and a Raspberry Pi 3 has been developed. First, the thermal images captured by the hardware system are processed to eliminate fixed interferences and identify the human body. Then, the real height of the human body is estimated from the original height in the thermal images. Finally, after smoothing the fluctuation of the real height, fall events are detected according to the relative variations of the smoothed height. Our experiments show that the newly developed system and image processing algorithm can achieve much better performance on fall detection than other systems based on infrared sensors or sensor arrays.

Index Terms-Fall detection, Thermopile imaging array, Back projection

I. INTRODUCTION

Nowadays, aging society becomes a major trend in most countries around the world, and the population aged 65 and over is increasing rapidly [1]. For elderly people, falls may cause serious injury and accidental death. What makes it even worse is that many elderly people are living alone, and may not be able to get up and request medical help in time after falling [2]. Therefore, fall detection systems become more and more important for both elderly people and caregivers.

Existing fall detection systems can be categorized into wearable sensing systems and non-wearable sensing systems. The wearable sensors include accelerometer [3], gyroscopes [4], capacitive sensors [5], and so on, which need to be worn on specific positions of a human body, such as arms, legs, waist, or chest, to sense body position and movement for fall detection. But wearing sensors all the time bring uncomfortable feelings and inconvenience to elderly people.

Non-wearable sensing systems are friendlier to elderly people. The typical fall detection devices include video cameras [6], floor vibration and pressure sensors [7], Doppler radar sensor [8], forward scattering radar [9], infrared sensor or sensor array [10-13], and so on. The video-based systems have high accuracy, but unavoidably the privacy of elderly people is badly invaded. For the systems based on floor vibration and pressure sensors, Doppler radar array, or microphone array, the accuracy on fall detection is poor.

Recently, more and more low-cost infrared sensors or sensor arrays, especially thermopile imaging arrays, become commercial off-the-shelf products. Their resolutions vary from 8*8, 16*16, 32*32, to 80*64 pixels [14-16]. On one hand, thermopile imaging arrays can capture rich activity information of elderly people and achieve high accuracy on fall detection; On the other hand, the captured thermal images have a much lower resolution as compared to video images, hence the privacy invasion issue is considerably alleviated. Therefore, developing fall detection systems with thermopile imaging arrays becomes a promising research direction.

In this paper, we have built a fall detection system consisting of a thermopile imaging array having 80*64 pixels and a Raspberry Pi 3, developed a back projection algorithm to obtain the real height of a human body from the original height in the thermal images, and proposed a fall detection criterion that can achieve much better performance than other systems based on infrared sensors or sensor arrays. The rest of the paper is organized as follows. Section II describes the installation of the thermopile imaging array, the back projection algorithm, and the fall detection criterion in detail. Section III presents and discusses fall detection results. Finally, conclusions are given in Section IV.

II. THERMOPILE ARRAY INSTALLATION, BACK PROJECT ALGORITHM, AND FALL DETECTION CRITERION

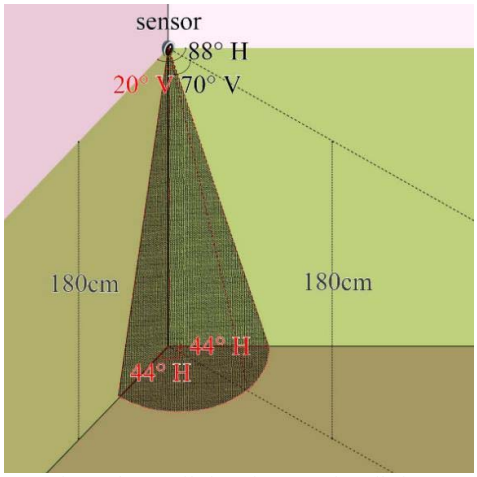

Fig. 1 Thermopile imaging array installation

In this research, we use HTPA80x64dR1L5.0/1.0 [16], a thermopile imaging array made by HEIMANN Sensor GmbH to capture thermal images. This array has a resolution of 80*64 pixels and a field of view (FOV) of 88 degrees*70

978-1-7281-5317-9/20/$31.00 ©2020 IEEE

degrees. As shown in Fig. 1, the array is installed in the corner of a room with 1.8 meters above the ground and the size of the room is about 5m*5m. To cover as many areas as possible, the 88-degree FOV is aligned with the horizontal direction, and 70-degree FOV is aligned with the vertical direction. As a result, the array can cover almost all areas lower than 1.8m in the room except the small shaded area in Fig. 1.

The flow chart of the fall detection procedure proposed by this paper is given in Fig. 2, and the image processing practices listed in the flow chart are discussed in detail as follows.

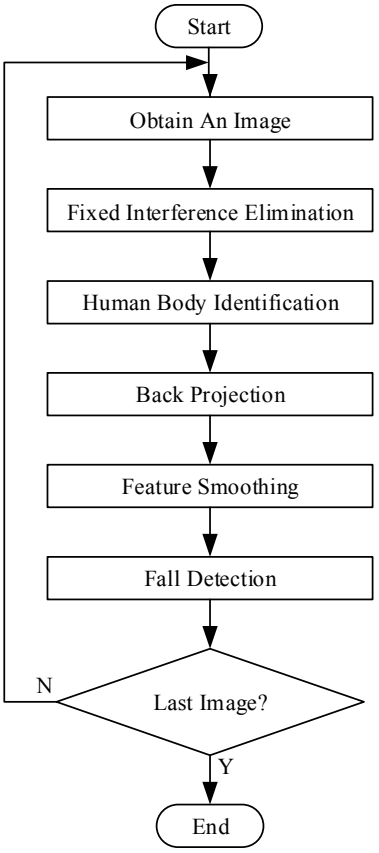

Fig. 2 Algorithm flow chart

2.1 Fixed Interference Elimination

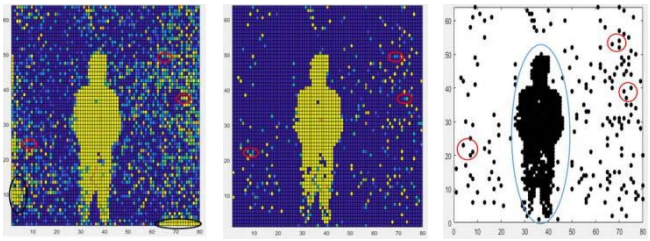

(a) Original Image (b) Processed Image (c) Connected Domains

Fig. 3 A thermal image and relative processing

An original image acquired by the thermopile imaging array is shown in Fig. 3(a), where pixels in yellow have a higher temperature than those in purple. The original images contain two different types of interferences: (1) Fixed interferences: marked with black circles in Fig. 3(a), those pixels have a high temperature in many consecutive images, which are typically caused by high-temperature unmovable subjects in the room. (2) Random interferences: marked with red circles in Fig. 3(a), the positions of those pixels vary randomly among consecutive images. The fixed interferences can be easily removed by using the method in [9], and an image after the interference elimination processing is shown in Fig. 3(b).

2.2 Human Body Identification

After eliminating the fixed interferences, the processed images are binarized, and all connected domains in every image are extracted by using the rule of 8-connected pixels. As shown in Fig. 3(c), besides the connected domain for a human body, there are many other connected domains caused by the random interferences. Typically, the connected domain for a human body has the largest pixel number or summed temperature. However, in some images, a connected domain caused by the random interferences may exceed that for a human body in pixel number or summed temperature. To enhance the accuracy of identifying the connected domain for a human body, we have developed the following image processing steps. Firstly, the summed temperature of $S_i(n)$, the i^{th} connected domain in nth processed image, is calculated as below:

$$T_i(n) = \sum_{p \in S_i(n)} Z_p(n), \tag{1}$$

where $Z_p(n)$ is the temperature of the p^{th} pixel in the n^{th} processed image. Then the coordinates of the center of gravity (CoG) of $S_i(n)$, $\{x_{c_i}(n), y_{c_i}(n)\}$, are obtained by:

$$\{x_{c_i}(n),\ y_{c_i}(n)\} = \frac{\sum_{p \in S_i(n)} Z_p(n)\ \{x_p(n),\ y_p(n)\}}{\sum_{p \in S_i(n)} Z_p(n)}, \tag{2}$$

where $\{x_p(n), y_p(n)\}$ are the coordinates of the p^{th} pixel in the n^{th} processed image.

If in the $(n\text{-}2)^{\text{th}}$ and $(n\text{-}1)^{\text{th}}$ images, the coordinates of the CoG of the connected domain for a human body are respectively $\{x(n\text{-}2),\ y(n\text{-}2)\}$ and $\{x(n\text{-}1),\ y(n\text{-}1)\}$, the coordinators of the CoG of the connected domain for a human body in the n^{th} image can be predicted as:

$$\{\hat{x}(n), \hat{y}(n)\} = \{2x(n-1) - x(n-2),\ 2y(n-1) - y(n-2)\}. \tag{3}$$

For the i^{th} connected domain, the distance between its real CoG and the predicted CoG is calculated and denoted as $d_i(n)$. Then the summed temperature of the connected domain is adjusted as follows:

$$\tilde{T}_i(n) = T_i(n) - K d_i(n), \tag{4}$$

where K is a constant. Finally, the connected domain with the largest $\tilde{T}_i(n)$ is identified as the one for a human body and denoted as $S(n)$. Our experiments show that when K=10, the accuracy of identifying the connected domain for a human body can reach 100%.

2.3 Back projection

Generally, we can detect a fall through measuring the height of a human body in the images. However, because of the installation approach shown in Fig. 1, the height of a human body in the thermal images varies considerably at different positions of the FOV. Consequently, detecting falls from the original height in the images may cause many errors. In order to get the real height of a human body from the original height, we need to develop a back projection algorithm to project the object in the thermal images back to the real world.

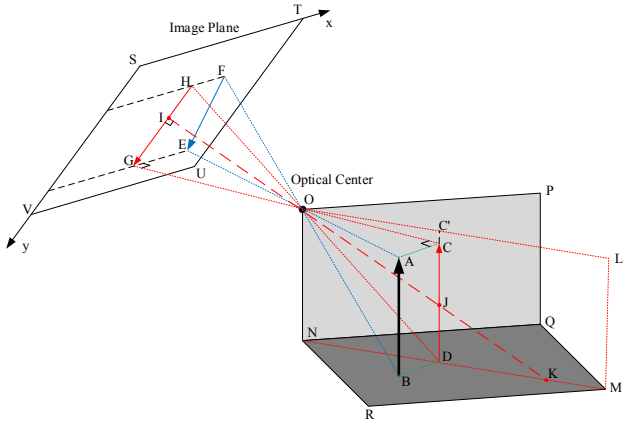

Fig.4 Schematic diagram of back projection

In Fig. 4, the black arrow AB stands for the real height of a human body, the blue arrow EF represents the image of the human body on the image plane, and the red arrow CD denotes the projection of the human body on the plane OLMN where the main optical axis of the thermopile imaging array is located. Obviously, we cannot work out the length of AB by only knowing the length of EF. First, we need to find the length of OA, namely the distance between the person and the thermopile imaging array. Through a large number of experiments, we found that the distance between the person and the thermopile imaging array can be estimated from the average temperature of the connected domain for a human body, T_{image}, with the following equation:

$$OA = -127 \times T_{image} + 5341, \tag{5}$$

where T_{image} is in ^{o}C and OA is in millimeter.

Second, in the thermal images, we use pixels as the unit of length. In order to measure the length in the real world, we need to convert pixels into millimeters. As shown in Fig. 5, f is the focal length of the thermopile imaging array, R_{ex} is the number of pixels of the thermopile imaging array in the horizontal direction, γ is the FOV of the sensor in the horizontal direction, R_{ey} is the number of pixels in the vertical direction, and φ is the FOV in the vertical direction.

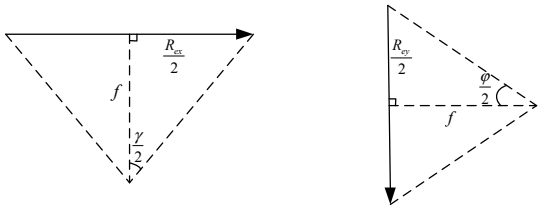

(a) unit conversion in horizontal direction (b) unit conversion in vertical direction

Fig.5 Schematic diagram of unit conversion

Therefore, the true length of each pixel in the horizontal direction, p_x (in mm/pixel), can be calculated by:

$$p_x = \frac{2f \times \tan\frac{\gamma}{2}}{R_{ex}}. \tag{6}$$

Similarly, the true length of each pixel in the vertical direction, p_x (in mm/pixel), can be calculated by:

$$p_y = \frac{2f \times \tan\frac{\varphi}{2}}{R_{ey}}. \tag{7}$$

Third, according to Fig. 4, GH is the projection of EF on the y-axis, and its length can be calculated by:

$$GH = p_y \times \left| y_E - y_F \right|, \tag{8}$$

where y_E and y_F represent the coordinate values of E and F in the y-axis direction, respectively.

Fourth, in Fig.4, IOK is the main optical axis of the thermopile imaging array, and I is the center of the plane STUV, OI is perpendicular to the plane STUV, and the length of OI is f, the focal length of the thermopile imaging array. Because the resolution of the thermopile imaging array is 80×64, the pixel coordinates of I are $\{x_I$=39.5, y_I=31.5$\}$.

In ΔOIG, because OI is vertical to IG, denoted as OI⊥IG, the length of OG can be calculated by:

$$OG = \sqrt{f^2 + \left[p_y \times (y_G - y_I)\right]^2} = \sqrt{f^2 + \left[p_y \times (y_E - y_I)\right]^2}. \tag{9}$$

Similarly, in ΔOIE, because OI⊥IE, the length of OE can be calculated by:

$$OE = \sqrt{f^2 + \left[p_x \times (x_E - x_I)\right]^2 + \left[p_y \times (y_E - y_I)\right]^2}. \tag{10}$$

In ΔOGE, because GE⊥OG, we can get

$$\angle EOG = \arccos\frac{OG}{OE}. \tag{11}$$

In ΔAOC, because AC⊥OC and ∠EOG and ∠AOC are vertical angles, the length of OC can be calculated by:

$$OC = OA \times \cos\angle AOC = OA \times \cos\angle EOG. \tag{12}$$

Fifth, the plane HGOCD extracted from Fig. 4 is shown in

Fig. 6 to demonstrate the relationship between CD and GH.

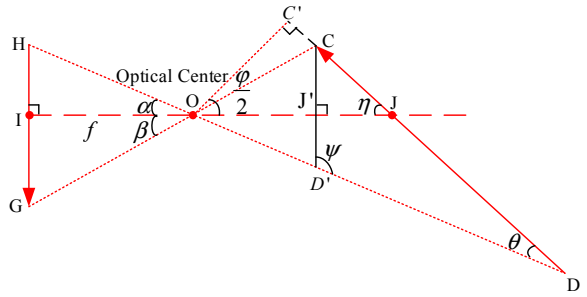

Fig. 6 Schematic diagram of back projection on plane HGOCD

Because OI⊥HI, we can get

$$\alpha = \arctan\frac{HI}{OI} = \arctan\frac{|y_H - y_I| \times p_y}{f} = \arctan\frac{2\times|y_F - y_I|\times\tan\frac{\varphi}{2}}{R_{ey}} \tag{13}$$

Similarly, because OI⊥GI, we can get

$$\beta = \arctan\frac{GI}{OI} = \arctan\frac{|y_G - y_I| \times p_y}{f} = \arctan\frac{2\times|y_E - y_I|\times\tan\frac{\varphi}{2}}{R_{ey}} \tag{14}$$

According to Figs. 1 and 4, ∠C'OJ=φ/2. Thus, we can get

$$\eta = 90° - \frac{\varphi}{2}. \tag{15}$$

Because η is an exterior angle of ΔOJD, we can get

$$\theta = \eta - \alpha. \tag{16}$$

Then considering ΔCD'D and ΔCJ'J, we can get

$$\psi = 90° + \alpha. \tag{17}$$

Furthermore, in ΔCJ'O, because CJ'⊥OJ', the length of OJ' can be calculated by:

$$OJ' = OC\times\cos\angle COJ' = OC\times\cos\beta. \tag{18}$$

Because ΔHOG and ΔD'OC are similar triangles, we can get

$$CD' = \frac{OJ'}{f}\times GH. \tag{19}$$

Meanwhile, according to the sine theorem, the length of CD can be calculated by:

$$CD = \frac{CD'\times\sin\psi}{\sin\theta}. \tag{20}$$

According to Fig. 4, CD is the projection of AB, the real height of a human body on the plane OLMN, and hence AB=CD.

Finally, by combining all the above equations together, we can get the real height of a human body from Eq. (21). This method can also be applied to calculate the real width of a human body if necessary.

2.4 Feature Smoothing

As shown in Fig. 7(a), the real height of a human body, $h(n)$, fluctuates significantly in several consecutive images. This fluctuation is mainly caused by the random interferences in the thermal images and the errors when estimating OA from T_{image} with Eq. (5). In order to reduce the fluctuation and improve the accuracy for fall detection, we have smoothed $h(n)$ through averaging over N consecutive images, i.e.

$$H(n) = \frac{1}{N}\sum_{i=n-N+1}^{n} h(i). \tag{22}$$

Because the thermopile imaging array captures 6~7 images

$$\begin{aligned} AB = CD &= \frac{OA\times\cos\left(\arccos\frac{\sqrt{f^2+\left[\frac{2f\times\tan\frac{\varphi}{2}}{R_{ey}}\times(y_E-y_I)\right]^2}}{\sqrt{f^2+\left[\frac{2f\times\tan\frac{\gamma}{2}}{R_{ex}}\times(x_E-x_I)\right]^2+\left[\frac{2f\times\tan\frac{\varphi}{2}}{R_{ey}}\times(y_E-y_I)\right]^2}}\right)\times\cos\left(\arctan\frac{2\times|y_G-y_I|\times\tan\frac{\varphi}{2}}{R_{ey}}\right)}{f} \times \frac{2f\times\tan\frac{\varphi}{2}}{R_{ey}}\times|y_E-y_F|\times\sin\left(90°+\arctan\frac{2\times|y_H-y_I|\times\tan\frac{\varphi}{2}}{R_{ey}}\right) \\ &= \frac{}{\sin\left(90°-\frac{\varphi}{2}-\arctan\frac{2\times|y_H-y_I|\times\tan\frac{\varphi}{2}}{R_{ey}}\right)} \\ &= \frac{2\times OA\times\sqrt{f^2+\left[\frac{2f\times\tan\frac{\varphi}{2}}{R_{ey}}\times(y_E-y_I)\right]^2}\times\cos\left(\arctan\frac{2\times|y_E-y_I|\times\tan\frac{\varphi}{2}}{R_{ey}}\right)\times\tan\frac{\varphi}{2}\times|y_E-y_F|\times\sin\left(90°+\arctan\frac{2\times|y_F-y_I|\times\tan\frac{\varphi}{2}}{R_{ey}}\right)}{\sqrt{f^2+\left[\frac{2f\times\tan\frac{\gamma}{2}}{R_{ex}}\times(x_E-x_I)\right]^2+\left[\frac{2f\times\tan\frac{\varphi}{2}}{R_{ey}}\times(y_E-y_I)\right]^2}\times R_{ey}\times\sin\left(90°-\frac{\varphi}{2}-\arctan\frac{2\times|y_F-y_I|\times\tan\frac{\varphi}{2}}{R_{ey}}\right)} \end{aligned} \tag{21}$$

per second, we set N=20 in our experiments so as to reduce the fluctuation but still maintain the feature information needed for fall detection. As shown in Fig. 7(b), after smoothing the fluctuation of the height has been mitigated considerably.

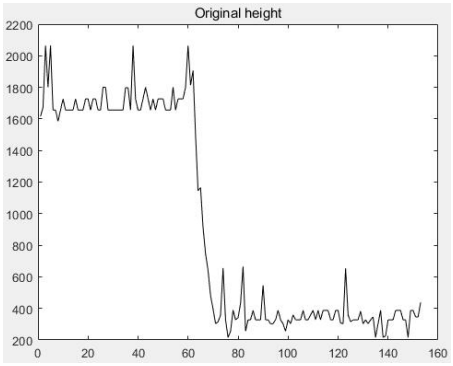

(a) Before smoothing

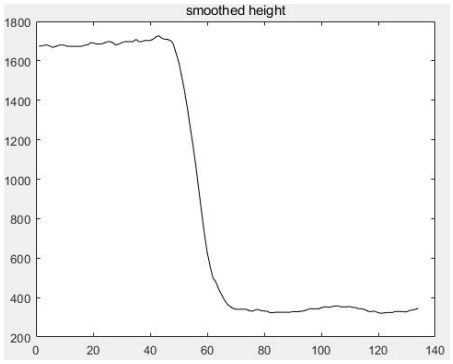

(b) After smoothing

Fig. 7 Smoothing real height of a human body

2.5 Fall Detection

After investigating numerous images captured by the thermopile imaging array sensor and many features extracted from those images, we found that considering the relative variations of the smoothed height, $H(n)$, can accurately distinguish a falling from standing, sitting, squatting, walking, and lying down, and can achieve very high accuracy on fall detection. Therefore, we have developed the following criterion for fall detection:

$$\frac{H(n)}{H(n-M)} < \mu. \tag{23}$$

When the criterion is satisfied, a fall is detected. Extensive investigations show that for our experiment settings the optimal values for M, μ are M=12 and μ=0.55.

III. Fall Detection Results And Discussions

To evaluate the performance of the fall detection system based on the thermopile imaging array sensor, we have collected thermal images for 100 fall events and 100 non-fall events and applied the fall detection algorithm developed by this paper to identify fall and non-fall events from those images. In addition to the accuracy, the other two performance indicators, sensitivity and specificity, have been used to evaluate the performance of the fall detection system. The sensitivity (also named as the true positive rate) measures the proportion of actual positives (corresponds to fall events) that are correctly classified. The specificity (also named as the true negative rate) measures the proportion of actual negatives (corresponds to non-fall events) that are correctly classified.

The accuracy, sensitivity, and specificity of the fall detection system based on back-projection are shown in Table 1. The performance of three other fall detection systems using infrared sensors or sensor arrays [11-13] is also listed in Table 1 for comparison purposes.

It can be concluded from Table 1 that the fall detection system and algorithm proposed in this paper can accurately identify all non-fall events, i.e. its specificity reaches 100%. Meanwhile, the sensitivity of the proposed system and algorithm reaches 98%. Both two fall events that were mistakenly identified as non-fall events have a similar situation: a human body falls in the direction of the optical axis of the thermopile imaging array sensor, and hence the relative variations of $H(n)$ are small and cannot fulfill the criterion set by Eq. (23). In our future research, this algorithm's weakness will be tackled. Otherwise, the proposed system and algorithm outperforms the other fall detection systems no matter on the accuracy, sensitivity, or specificity. Furthermore, it is worth mentioning that the proposed system only applies one array, while others apply multiple sensors or sensor arrays, which increases both hardware and installation complexity.

Table 1 Comparison of fall detection systems

	Our research	[11]	[12]	[13]
Number of Fall	100	80	40	40
Number of Non-Fall	100	80	200	160
Sensitivity (%)	98	95.25	92.5	86.5
Specificity (%)	100	90.75	93.7	97.97
Accuracy (%)	99	93	93.5	95.67

IV. Conclusions

In this paper, a fall detection system consisting of a thermopile imaging array having 80*64 pixels and a Raspberry Pi 3 has been built. The thermal images captured by the hardware system are processed to eliminate fixed interferences, identify the human body, estimate the real height of the human body through a back projection algorithm, and smooth the fluctuation of the real height. Finally, fall events are detected according to the criterion obtained from extensive experiments. The fall detection results show that the newly developed system and image

processing algorithm can achieve much better fall detection performance on sensitivity, specificity, and accuracy than other systems based on infrared sensors or sensor arrays.

REFERENCES

[1] D. Bloom, D. Canning, and A. Lubet, "Global Population Aging: Facts, Challenges, Solutions & Perspectives". Daedalus, 80-92, April 2015.
[2] N. El-Bendary, Q. Tan, F.C. Pivot, and A. Lam, "Fall Detection and Prevention for the Elderly: A Review of Trends and Challenges", International Journal on Smart Sensing and Intelligent Systems, Vol. 6, No. 3, pp. 1230-1266, June 2013.
[3] J. Lee, and H. Tseng, "Development of an Enhanced Threshold-Based Fall Detection System Using Smartphones With Built-In Accelerometers", IEEE Sensors Journal, Vol. 19, No. 18, pp. 8293-8302, Sep. 2019.
[4] D. Giuffrida, G. Benetti, D. De Martini, T. Facchinetti, "Fall Detection with Supervised Machine Learning using Wearable Sensors," Proceedings of 2019 IEEE 17th International Conference on Industrial Informatics (INDIN), pp. 253-259, July 2019.
[5] S. Bian, V. F. Rey, J. Younas, and P. Lukowicz, "Wrist-Worn Capacitive Sensor for Activity and Physical Collaboration Recognition", Proceedings of 2019 IEEE International Conference on Pervasive Computing and Communications Workshops (PerCom Workshops), pp. 261-266, March 2019.
[6] Evelien E.Geertsema, Gerhard H.Visser, Max A.Viergever and Stiliyan N.Kalitzin, "Automated remote fall detection using impact features from video and audio," Journal of Biomechanics, Vol.88, pp. 25-32, May 2019.
[7] O. Noriyuki, Y. Yusuke, K. Ryu and Y. Osamu, "Fall detection and walking estimation using floor vibration for solitary elderly people", Proceedings of 2019 IEEE International Conference on Systems, Man and Cybernetics (SMC), pp. 1437-1442, Oct. 2019.
[8] Y. Haruka, M. Vasily, and H. Koji, "Fall Detection on a single Doppler Radar Sensor by using Convolutional Neural Networks", Proceedings of 2019 IEEE International Conference on Systems, Man and Cybernetics (SMC), pp. 2889-2892, Oct. 2019.
[9] Alnaeb, Ali and raja abdullah, raja syamsul azmir and Salah, Asem and Sali, Aduwati and Rashid, Nur and Pasya, Idnin, "Detection and classification Real-Time of Fall Events from the Daily Activities of Human Using Forward Scattering Radar", Proceedings of 2019 20th International Radar Symposium (IRS), pp. 1-10, June 2019.
[10] Q. Liang, L. Yu, X. Zhai, Z. Wan, and H. Nie, "Activity Recognition Based on Thermopile Imaging Array Sensor," Proceedings of 2018 IEEE International Conference on Electro/Information Technology (EIT2018), Rochester, MI, May 2018.
[11] W Chen and H. Ma, "A fall detection system based on infrared array sensors with tracking capability for the elderly at home," Proceedings of IEEE 18th International Conference on e-Health Networking, Applications and Services (Healthcom2016), Munich, Germany, Sept. 2016.
[12] T. Liu, X. Guo, and G. Wang, "Elderly-falling detection using distributed direction-sensitive pyroelectric infrared sensor arrays," Multidimensional Systems and Signal Processing, Vol. 23, No. 4, pp. 451-467, 2012.
[13] X. Luo, T. Liu, J. Liu, X. Guo, and G. Wang, "Design and implementation of a distributed fall detection system based on wireless sensor networks," EURASIP Journal on Wireless Communications and Networking, 2012:118, Dec. 2012.
[14] HTPA8x8d, Retrieved from http://www.heimannsensor.com/Datasheets/Overview-HTPA8x8d_Rev3.pdf
[15] HTPA32x32d, Retrieved from http://www.heimannsensor.com/Datasheets/Overview-HTPA32x32d_Rev3.pdf
[16] HTPA80x64d, Retrieved from http://www.heimannsensor.com/Datasheets/Overview-HTPA80x64d_Rev8.pdf